A 3D-1D MODEL FOR THE SIMULATION OF PLANT-SCALE CHEMICAL REACTORS

RICCARDO TOGNI[1], ALICE HAGER[1], CHRISTOPH KLOSS[1] AND CHRISTOPH GONIVA[1]

[1]DCS Computing GmbH
Industriezeile 35, 4020 Linz, Austria
E-mail: riccardo.togni@dcs-computing.com, web page: http: //www.aspherix-dem.com

Key words: CFD-DEM, immersed boundary method, reduced order model, methane reactor

Abstract. A 3D-1D model for simulating the methane dehydroaromatization (MDA) process in catalytic reactors is here presented. The 3D part of the model consists of CFD-DEM coupled simulations of some relevant volume elements (RVEs), while the 1D part is a low-order model bridging the solution between the RVEs. The CFD-DEM model, implemented in the CFDEM®coupling and Aspherix® software, uses an immerse boundary method to resolve: 1) the flow around the catalytic structures, 2) the heat exchange between solid and fluid, 3) the MDA reaction at the fluid-catalyst interface. The CFD-DEM solution is scaled-up by the 1D model to allow the simulation of industrial-scale processes at acceptable computational cost. The effect of the catalyst structure's size and reactor operating temperature on the methane conversion rate and pressure drop are investigated using the proposed model.

1 INTRODUCTION

Non-oxidative methane dehydroaromatization (MDA) is one of the most promising processes for the direct conversion of methane into hydrogen and high-value aromatics (mainly benzene) [1, 2]. In a typical MDA reactor, high-temperature methane is pumped through a porous structure coated with a catalyst. The yield of the reactor, measured in terms of methane conversion, is influenced by multiple factors such as the operating conditions (e.g., temperature of the gas), geometry of the structure and chemical properties of the catalyst. While many studies have focused on assessing the thermodynamic performances of catalyst materials, little attention has been paid to the fluid dynamics aspect of the problem [3, 4]. The geometry of the catalyst plays a crucial role in the reactor design. For example, an increase of the catalyst porosity leads to higher surface area and thus faster methane conversion; however, a denser catalytic structure involves higher pressure losses and, therefore, more power is required to operate the reactor.

In this work, a 3D-1D model capable to simulate the MDA process in reactors from lab- to plant-scale is presented. The focus lies on the fluid dynamics behaviour of the system and, in particular, the effect of catalyst structure's size and operating temperature on the methane conversion and pressure drop. The MDA is modelled by considering only the main reaction, namely the reversible decomposition of methane (CH_4) into hydrogen (H_2) and benzene (C_6H_6):

$$6\,CH_4 \;\leftrightarrows\; C_6H_6 + 9\,H_2. \tag{1}$$

The reactor, which is assumed to have a tubular shape, is simulated by means of a combined

3D-1D approach. The 3D part consists of particle-resolved CFD-DEM simulations of some reactor sections, while the 1D part consist of a low-order model that bridges the solution between the sections. This approach allows, on the one hand, to fully-resolve the flow through the porous catalyst material and, on the other, to limit the computational cost by reducing the size of CFD-DEM simulation domains to a minimum and use an inexpensive low-order model to interpolate the solution between the sections.

The model uses Aspherix® and CFDEM®coupling engines to solve the mass, momentum, energy transport and reaction kinetics in the particle-resolved CFD-DEM simulations. Aspherix® is a commercial DEM software developed by DCS Computing and successor of the open-source code LIGGGHTS® [5], while CFDEM®coupling is a parallel coupled CFD-DEM framework combining the strengths of Aspherix® and the Open Source CFD package OpenFOAM® [6]. This paper is organized as follows: the 3D-1D model is described in Section 2, followed by the simulation results in Section 3, and the conclusions in Section 4.

2 MODELLING APPROACH

The catalytic reactor is modelled by means of a combined 3D-1D approach. The 3D part of the model consists of particle-resolved CFD-DEM simulations of some Representative Volume Elements (RVEs), while the 1D part consists of a low-order model connecting the RVEs, as sketched in Figure 1a.
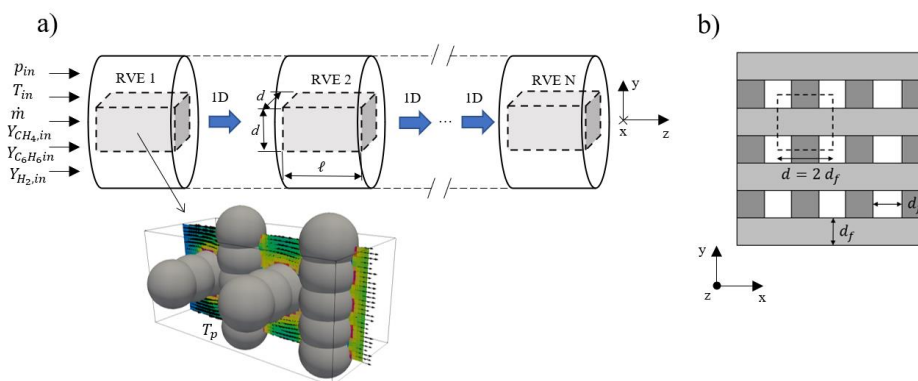

Figure 1: a) sketch showing the discretization of the reactor domain into RVEs connected by 1D models. The lower inset shows the results of a particle-resolved CFD-DEM simulation of an RVE. (b) Sketch of the straight-channel configuration of the catalyst structure.

Each RVE represents a section of the reactor and consists of two regions: a solid catalyst structure, which is modelled by a fibre network, and a fluid domain. Each fibre is made of overlapping DEM spheres having a diameter d_f; see the lower inset in Figure 1a. The catalyst geometry that has been considered in this study is the straight-channel configuration shown in Figure 1b. Due the periodicity of the straight-channel geometry, the lateral size d of each RVE is set to two-times the fibre diameter d_f and periodic boundary conditions are imposed along x and y directions to account for the larger lateral extension of each section. The longitudinal size ℓ of the RVEs is set to four-times the fibre diameter in order to resolve the flow inhomogeneity across two catalyst layers, where each layer consists of two orthogonal fibres. The CFD

boundary conditions to be specified at the reactor's inlet are the gas flow rate $\dot{m}$, temperature T_{in}, pressure p_{in}, the mass concentration of methane $Y_{CH4,in}$, hydrogen $Y_{H2,in}$ and benzene $Y_{C6H6,in}$. The DEM particles have a constant temperature T_p in all the RVEs, which ensures a constant operating temperature of the gas along the reactor if $T_{in} = T_p$. The governing equations of the 3D model are presented in Section 2.1, followed by a description of the reaction kinetics modelling in Section 2.2 and of the 1D model in Section 2.3.

2.1 Resolved CFD-DEM simulation

Resolved CFD-DEM simulations are applied to problems where the immersed solid bodies are much larger than the mesh size discretizing the fluid field. The modelling approach presented here is a fictitious domain method, which consists in discretizing and solving the governing equations of the fluid over the entire domain, while the mass, momentum and energy exchange between solid and fluid phases are set by specific boundary conditions on the regions covered by the solid bodies [5, 7]. On the DEM side, the momentum and energy equations of the solid bodies are coupled to the continuum model and solved.

Before introducing the governing equations, let us consider a simplified version of the problem, consisting of a single spherical particle immersed in a fluid; see Figure 2. The total domain Ω can be split into two parts: a fluid domain Ω_f and a solid domain Ω_s, where Γ_s denotes the boundary between fluid and solid.
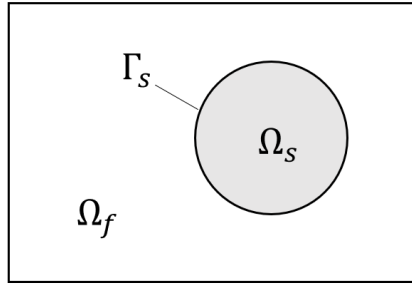

Figure 2: decomposition of the domain in a fictitious domain method.

By referring to this domain compositions, the governing equations of a compressible reacting multi-species fluid mixture are the following continuity, momentum, energy and species concentration equations:

$$\frac{\partial \rho}{\partial t} + \nabla \cdot (\rho \boldsymbol{u}) = 0 \quad on\ \Omega, \tag{2}$$

$$\frac{\partial (\rho \boldsymbol{u})}{\partial t} + \nabla \cdot (\rho \boldsymbol{u} \otimes \boldsymbol{u}) = \nabla \cdot \boldsymbol{\sigma} + \rho \boldsymbol{g} \quad on\ \Omega, \tag{3}$$

$$\frac{\partial (\rho E)}{\partial t} + \nabla \cdot (\rho \boldsymbol{u} E) + \nabla \cdot (\boldsymbol{u} p) = -\nabla \cdot \boldsymbol{q} + \nabla \cdot (\boldsymbol{\tau} \cdot \boldsymbol{u}) + \rho \boldsymbol{g} \cdot \boldsymbol{u} + s_{E,c} + s_{E,p} \quad on\ \Omega, \tag{4}$$

$$\frac{\partial (\rho Y_i)}{\partial t} + \nabla \cdot (\rho Y_i \boldsymbol{u}) = \nabla \cdot \left(\alpha_i \nabla (\rho Y_i) \right) + s_{Y_i} \quad on\ \Omega. \tag{5}$$

Here, ρ is the density of the fluid mixture, $\boldsymbol{u}$ is the fluid velocity, $\boldsymbol{\sigma} = \mathbf{I}p + \boldsymbol{\tau}$ is the stress tensor, $\mathbf{I}$ is the identity tensor, p is the pressure, $\boldsymbol{\tau}$ is the shear stress tensor and $\boldsymbol{g}$ is the gravity acceleration. In the energy equation, E denotes the total energy, $\boldsymbol{q}$ is the heat flux, $s_{E,c}$ is the energy source due to chemical reaction and $s_{E,p}$ is the conductive heat exchange between particle and fluid. By assuming the presence of m species in the mixture, Y_i denotes the mass concentration of the ith-species, α_i is the mass diffusivity and s_{Y_i} is the mass concentration source due to chemical reaction. Equations 2-5 are closed by the following boundary conditions:

$$\boldsymbol{u} = \boldsymbol{u_p} \ \ on \ \Omega_s \ \ and \ \ \boldsymbol{\sigma} \cdot \hat{\boldsymbol{n}} = \boldsymbol{t_{\Gamma_s}} on \ \Gamma_s, \tag{6}$$

$$T = T_p \ \ on \ \Omega_s, \tag{7}$$

$$\sum_{i=1}^{m} Y_i = 1 \ \ on \ \Omega, \tag{8}$$

where $\boldsymbol{u_p}$ is the velocity of the particle, $\hat{\mathbf{n}}$ is the unit vector normal to the particle-fluid interface Γ_s, $\boldsymbol{t_{\Gamma_s}}$ is the stress vector exerted by the particle on the fluid and T_p is the particle temperature. Equation 6 and 7 establish the momentum and energy coupling between fluid and particle, while Equation 8 bounds the sum of the species mass concentrations to 1.

The evolution of the particle's velocity and temperature are governed by Equation 9 and 10, respectively. The former is the Newton's second-law of motion, where m_p is the particle's mass and $\boldsymbol{f_j}$ is the inter-particle force exerted by the generic jth-particle (where n is the total number of particles in contact, which in the example from Figure 2 is equal to zero). Equation 10 is the particle's energy equation, where c_p is the particle's heat capacity, $\boldsymbol{q_j}$ is the inter-particle heat flux from the generic jth-particle in contact, k is the fluid heat conductivity and ∇T the temperature gradient of the fluid. The integral term in Equation 9 is the force exerted by the fluid on the particle, while the integral term in Equation 10 is the total heat flux absorbed by the particle from the fluid.

$$m_p \frac{\mathrm{d}\boldsymbol{v_p}}{\mathrm{d}t} = m_p \boldsymbol{g} + \sum_{j=1}^{n} \boldsymbol{f_j} - \int_{\Gamma_s} \boldsymbol{t_{\Gamma_s}} \mathrm{d}\Gamma_s, \tag{9}$$

$$m_p c_p \frac{\mathrm{d}T_p}{\mathrm{d}t} = \sum_{j=1}^{n} \boldsymbol{q_j} - \int_{\Gamma_s} k\nabla T \cdot \hat{\mathbf{n}} \, \mathrm{d}\Gamma_s. \tag{10}$$

By considering the boundary condition in Equation 6 and by applying the divergence theorem, the integral term in Equation 9 can be rewritten as follows:

$$\int_{\Gamma_s} \boldsymbol{t_{\Gamma_s}} \mathrm{d}\Gamma_s = \int_{\Gamma_s} \boldsymbol{\sigma} \cdot \hat{\mathbf{n}} \, \mathrm{d}\Gamma_s = \int_{\Omega_s} \nabla \cdot \boldsymbol{\sigma} \, \mathrm{d}\Omega_s. \tag{11}$$

Similarly, the integral term in Equation 10 can be expressed as:

$$\int_{\Gamma_s} k\nabla T \cdot \hat{\mathbf{n}} \, \mathrm{d}\Gamma_s = \int_{\Omega_s} k\nabla^2 T \, \mathrm{d}\Omega_s, \tag{12}$$

where k is assumed to be constant. By recalling Equation 4, where the total conductive heat exchange between particle and fluid was defined as $s_{E,p}$, it follows that:

$$s_{E,p} = \int_{\Omega_s} k\nabla^2 T \, d\Omega_s. \tag{13}$$

In conclusion, the momentum and energy coupling terms between CFD and DEM equations can be obtained by integrating the divergence of the fluid's stress tensor (Equation 9, 11) and the divergence of conductive heat flux (Equation 10, 12) over the solid domain Ω_s.

2.2 Modelling of reaction kinetics

The chemical species involved in the reaction are methane (CH_4), hydrogen (H_2) and benzene (C_6H_6); see Equation 1. In order to model the chemically-inert interior of the catalyst structure, the inactive species nitrogen (N_2) is added to fill in the solid domain Ω_s. In order to prevent the transport of N_2 outside Ω_s, the nitrogen mass diffusivity is set artificially to zero. The resulting species concentration equations are:

$$\frac{\partial(\rho Y_{CH_4})}{\partial t} + \nabla \cdot (\rho Y_{CH_4} \boldsymbol{u}) = \nabla \cdot \left(\alpha_{CH_4} \nabla(\rho Y_{CH_4})\right) + s_{Y_{CH_4}} \quad on \ \Omega, \tag{12}$$

$$\frac{\partial(\rho Y_{H_2})}{\partial t} + \nabla \cdot (\rho Y_{H_2} \boldsymbol{u}) = \nabla \cdot \left(\alpha_{H_2} \nabla(\rho Y_{H_2})\right) + s_{Y_{H_2}} \quad on \ \Omega, \tag{13}$$

$$\frac{\partial(\rho Y_{C_6H_6})}{\partial t} + \nabla \cdot (\rho Y_{C_6H_6} \boldsymbol{u}) = \nabla \cdot \left(\alpha_{C_6H_6} \nabla(\rho Y_{C_6H_6})\right) + s_{Y_{C_6H_6}} \quad on \ \Omega, \tag{14}$$

$$\frac{\partial(\rho Y_{N_2})}{\partial t} + \nabla \cdot (\rho Y_{N_2} \boldsymbol{u}) = 0 \quad on \ \Omega. \tag{15}$$

The initial condition chosen for the species concentration equations are:

$$Y_{CH_4}(t=0) = 1 \ on \ \Omega_f \ and \ Y_{CH_4}(t=0) = 0 \ on \ \Omega_s, \tag{16}$$

$$Y_{C_6H_6}(t=0) = 0 \ on \ \Omega_f \ and \ Y_{C_6H_6}(t=0) = 0 \ on \ \Omega_s, \tag{17}$$

$$Y_{H_2}(t=0) = 0 \ on \ \Omega_f \ and \ Y_{H_2}(t=0) = 0 \ on \ \Omega_s, \tag{18}$$

$$Y_{N_2}(t=0) = 0 \ on \ \Omega_f \ and \ Y_{N_2}(t=0) = 1 \ on \ \Omega_s. \tag{19}$$

The mass concentration sources $s_{Y_{CH_4}}$, $s_{Y_{H_2}}$ and $s_{Y_{C_6H_6}}$ are defined as follows:

$$s_{Y_{CH_4}} = -6 \, M_{CH_4}\left(k_f[CH_4]^\alpha - k_r[H_2]^\beta[C_6H_6]^\gamma\right), \tag{20}$$

$$s_{Y_{H_2}} = 9 \, M_{H_2}(k_f[CH_4]^\alpha - k_r[H_2]^\beta[C_6H_6]^\gamma), \tag{21}$$

$$s_{Y_{C_6H_6}} = M_{C_6H_6}\left(k_f[CH_4]^\alpha - k_r[H_2]^\beta[C_6H_6]^\gamma\right), \tag{22}$$

where M_{CH_4}, M_{H_2} and $M_{C_6H_6}$ are the molar masses of the species, k_f and k_r are the reaction rate constant of the forward and backward reactions, α, β and γ are the partial orders of reaction, $[CH_4]$, $[H_2]$ and $[C_6H_6]$ are the molar concentrations of the species. In what follows, it is

assumed for simplicity that the partial orders of reaction are equal to the corresponding stoichiometric coefficients, i.e., $\alpha = 6$, $\beta = 9$ and $\gamma = 1$. By recalling the reaction in Equation 1, it can be easily demonstrated that the sum of Equation 20, 21 and 22 is equal to zero, which means that the mass of consumed methane is entirely converted into hydrogen and benzene.

The forward reaction rate constant is calculated based on the Arrhenius equation:

$$k_f = A\,e^{-\frac{T_a}{T}}, \tag{23}$$

where A is the pre-exponential factor and T_a is the activation temperature. The units of k_f and A are, in this case, $s^{-1}mol^{1-\alpha}m^{3(\alpha-1)}$. In order to limit the MDA reaction only to the surface of the catalyst structure, the forward reaction rate is set to zero in the CFD cells not crossing the fluid-solid interface, i.e., for $x \notin \Gamma_s$. The backward reaction rate is calculated as follows:

$$k_r = \frac{k_f}{K_c}, \tag{24}$$

where K_c is the equilibrium constant. In what follows, we consider the equilibrium constant to be an exponential function of the temperature with the following form:

$$K_c = a\,e^{b\,T}, \tag{25}$$

where a and b are user-defined coefficients that can be obtained, for example, by fitting experimental data.

The model of the reaction kinetics depends on three parameters, namely the pre-exponential factor A, the activation temperature T_a, and the equilibrium constant's fitting coefficients a and b. As the calibration of the reaction kinetics models goes beyond the purpose of this work, the parameters have been obtained by combing information from literature [8, 9] and from consortium partners within the Zeocat-3D project [10]. The numerical value of the model parameters, as well as the simulation results obtained with them, are reported in Section 3.

2.3 The 1D model

The 1D model is used to interpolate one RVE solution to the next one, bridging the gap between the RVEs. The CFD fields that are interpolated are the mass concentrations of the reactive species (Y_{CH_4}, $Y_{C_6H_6}$ and Y_{H_2}), the gas pressure (p) and the temperature (T). The model linearly interpolates the inlet and outlet species mass concentrations at the ith RVE to obtain the inlet boundary condition for the (i+1)th RVE; see Figure 3a. A different interpolation type, namely a segmented linear regression, is used for p and T in order to damp unwanted fluctuations. As shown in Figure 3b, the model linearly interpolates the average p and T at the (i-1)th RVE and ith RVE to obtain the inlet boundary condition for the (i+1)th RVE.

The 1D model is called automatically when the 3D simulation of the RVE has reached a steady-state condition, namely when the volume-average of the fields does not significantly change over time. Since the interpolated mass concentrations might not fulfil anymore the boundary condition specified in Equation 8, the 1D model includes a normalization step that ensures that the sum of the interpolated mass concentrations is equal to one.
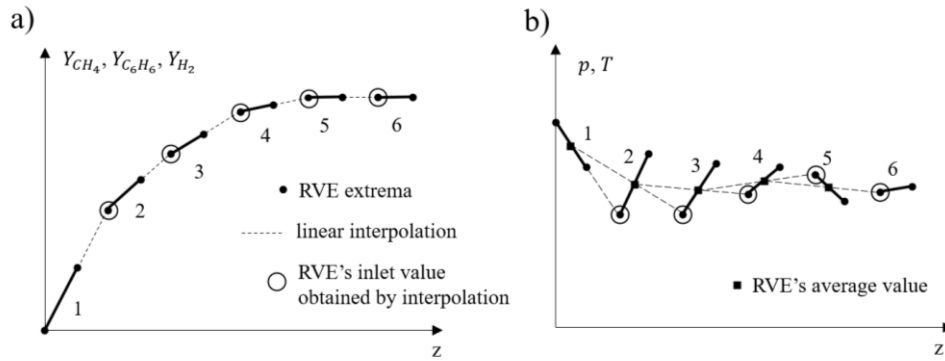
Figure 3: schematic representation of the 1D model using a) linear interpolation and b) segmented linear regression to calculate the inlet boundary conditions for the next RVE.

3   RESULTS AND DISCUSSION

This section presents two relevant results of the 3D-1D model. The first one is a simulation of a reactor with catalyst size $d_f = 0.4$ mm operating at three different temperatures ($T_{in} = T_p = 873$, 923 and 973 K), while the second is a simulation of a reactor with two different catalyst sizes ($d_f = 0.4$ and 0.8 mm) operating at the same temperature $T_{in} = T_p = 873$ K. The reason for choosing these two simulation groups is to study separately the effect of temperature and catalyst size on the reactor flow and to assess the capability of 3D-1D model to reproduce the main complexities of the system. Both reactor and catalyst geometries are the ones represented in Figure 1, while the simulation parameters are collected in Table 1 and Table 2.

The reactor length L is set in both cases equal to 0.1 m, as the reaction equilibrium is reached in the first centimetres of the reactor; see Figure 5 a-c. The fibre diameters d_f, as well as the mass flow rate $\dot{m}$ and inlet temperatures T_{in}, have been reasonably estimated by the authors based on the literature evidences and suggestions from consortium partners in the framework of the Zeocat-3D project. The reactors have been discretized with $N \approx 0.5(L/\ell)$ RVE's, which has been proved to be a good tradeoff between accuracy and simulation time.

Table 1: parameters of the simulations operating at three different temperatures.

L	0.1 m	p_{in}	$1.013\cdot10^{-5}$ Pa	$Y_{C6H6,in}$	0	T_a	25148 K
d_f	$0.4\cdot10^{-3}$ m	T_{in}	873.15 K, 923.15 K, 973.15 K	$Y_{CH4,in}$	1	a	$3.7063\cdot10^{-49}$
ℓ	$1.6\cdot10^{-3}$ m	T_p	873.15 K, 923.15 K, 973.15 K	$Y_{H2,in}$	0	b	$7.7320\cdot10^{-2}$
N	30	$\dot{m}$	0.0017 kg m^{-2}s^{-1}	A	$3.1\cdot10^{22}$ s^{-1}		

Table 2: parameters of the simulations with two different catalyst sizes.

L	0.1 m	p_{in}	$1.013\cdot10^{-5}$ Pa	$Y_{C6H6,in}$	0	T_a	25148 K
d_f	$0.4\cdot10^{-3}$ m, $0.8\cdot10^{-3}$ m	T_{in}	873.15 K	$Y_{CH4,in}$	1	a	$3.7063\cdot10^{-49}$
ℓ	$1.6\cdot10^{-3}$ m, $3.2\cdot10^{-3}$ m	T_p	873.15 K	$Y_{H2,in}$	0	b	$7.7320\cdot10^{-2}$
N	30, 15	$\dot{m}$	0.0017 kg m^{-2}s^{-1}	A	$3.1\cdot10^{22}$ s^{-1}		

Figure 4 shows two sections of velocity magnitude and benzene mass concentration fields at two yz-planes. This result has been obtained from the first simulation group at temperature 973.15 K and refers to the first RVE (see RVE 1 in Figure 1a). The mesh is adequately refined in proximity of the particles to resolve the boundary layer and relatively coarse away from the interface. The periodic boundary conditions in the x and y directions accounts for a larger lateral domain, while two layers of fibres are packed along z so that the draft of the upstream fibres influences the flow around the downstream fibres; see Figure 4a-b. Finally, a halo of benzene can be seen around the particles in Figure 4c-d. This is due to the fact that the chemical reaction is limited to the solid-fluid interface in order to properly model a catalytic reaction.
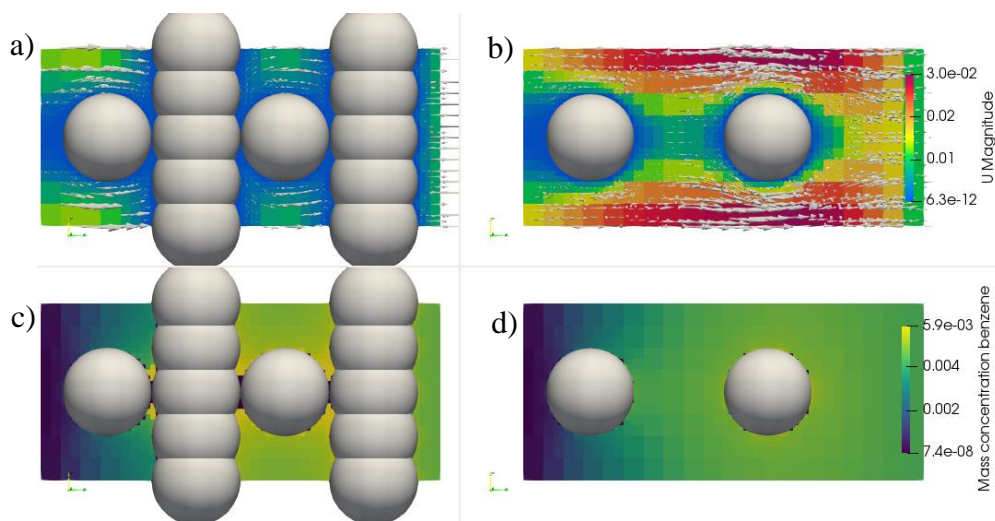

Figure 4: section of (a, b) velocity and (c, d) benzene mass concentration (a, c) in the middle of the RVE, i.e., x=0 mm, and (b, d) at x=0.8 mm. The result has been obtained from the simulation with catalyst size $d_f = 0.8$ mm and operating temperature $T = 873$ K (see Table 2).

3.1 Simulation with different operating temperatures

Figure 5 shows the main results of the reactor simulations conducted at three operating temperatures: 873.15, 923.15 and 973.15 K. As can be seen in Figure 5b, the methane conversion rate at the reactor's inlet, measured by the slope of Y_{CH_4} at $z = 0$, monotonically increases as a function of the operating temperature. The conversion rate becomes zero few centimeters downstream of the reactor's inlet, as Y_{CH_4} becomes constant, indicating the reach of the reaction equilibrium. The maximum methane conversion reached at the equilibrium clearly increases with the temperature and this behavior can be controlled by changing the coefficients a and b in the equilibrium constant definition; see Equation 25. A decrease in methane concentration corresponds to an increase in hydrogen and benzene concentrations, while their sum remains constant and equal to one along the reactor; see also Figure 5a and c.

The gas mixture is modelled as a perfect gas; hence, an isobaric increase of the temperature leads to lower gas densities. Since the mass flow rate $\dot{m}$ is constant, lower densities imply higher average velocities along the reactor; this behavior can be seen in Figure 5d. The average pressure along the reactor, represented in Figure 5e, decreases linearly with z and seems to be temperature-independent. A closer inspection of the data reveals that higher operating temperatures correspond to higher pressure drops (the difference is barely visible in the plot).

This behavior is to be expected, as higher average velocities correspond to higher drag forces and, therefore, higher pressure losses.
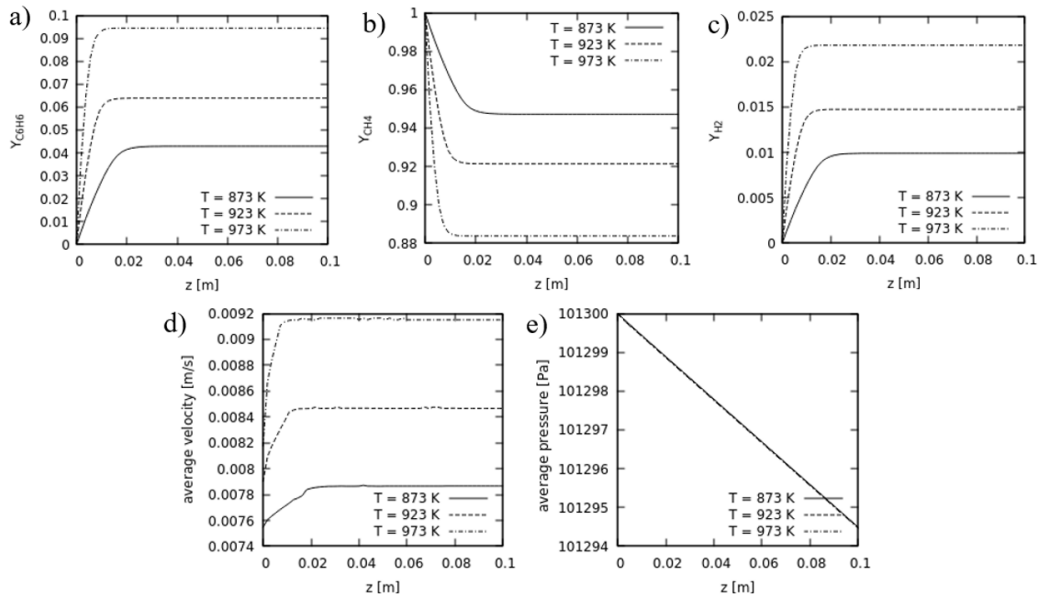

Figure 5: a) benzene, b) methane, c) hydrogen mass concentration, d) average velocity and e) pressure along the reactor length.

3.2 Simulation with different catalyst sizes

Figure 6 shows the main results of the reactor simulations conducted with two catalyst sizes: 0.4 and 0.8 mm. As can be seen in Figure 6a, a finer catalyst structure corresponds to a higher conversion rate, since the slope of $Y_{C_6H_6}$ at $z = 0$ for $d_f = 0.4$ mm is higher than the one for $d_f = 0.8$ mm. The average velocity along the reactor, represented in Figure 6b, does not show a clear effect of the catalyst size, while the average pressure, represented in Figure 6c, shows that a finer catalyst leads to higher pressure loss per unit length.
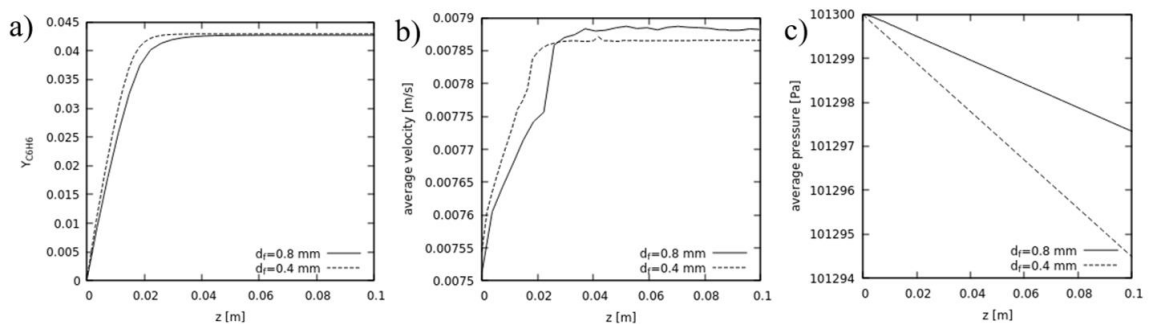

Figure 6: a) benzene mass concentration, b) average velocity and c) pressure along the reactor length.

4 CONCLUSIONS

This work presents a 3D-1D model for simulating the flow in MDA reactors. The 3D simulation of some relevant sections of the reactor using a particle-resolved CFD-DEM

simulation allows to accurately solve the physics of the problem, while the 1D model connects the 3D solutions together and enables the simulation of industrial-relevant problems with reasonable computational resources.

The particle-resolved CFD-DEM simulation uses an immerse boundary method to resolve the flow around the catalytic structures, the heat exchange between solid and fluid, and the MDA reaction at the fluid-catalyst interface. The MDA is modelled as a reversible methane decomposition into hydrogen and benzene, where the reaction rates are expressed via the Arrhenius equation and a user-defined equilibrium constant. Although the relative simplicity of the MDA model, the main features of the reactor flow seem to be captured, namely the temperature dependence of the conversion rate and maximum methane conversion, and the dependence of the pressure loss on the size of the catalyst structure.

Future studies will be devoted to the calibration of the model parameters and the validation of the model with the support of experimental results.

ACKNOWLEDGEMENT

REFERENCES

[1] U. Menon, M. Rahman and K. J. Khatib, "A Critical Literature Review of the Advances in Methane Dehydroaromatization over Multifunctional Metal-Promoted Zeolite Catalysts," *Applied Catalysis A: General,* no. 117870, 2020.

[2] K. Sun, D. M. Ginosar, T. He, Y. Zhang, M. Fan and R. Chen, "Progress in Nonoxidative Dehydroaromatization of Methane in the Last 6 Years," *Industrial & Engineering Chemistry Research,* vol. 57, no. 6, pp. 1768-1789, 2018.

[3] Z. Zhu, N. Al-ebbinni, R. Henney, C. Yi and R. Barat, "Extension to multiple temperatures of a three-reaction global kinetic model for methane dehydroaromatization," *Chemical Engineering Science,* vol. 177 , pp. 132-138, 2018.

[4] C. Karakaya, S. H. Morejudo, H. Zhu and K. J. Kee, "Catalytic chemistry for methane dehydroaromatization (MDA) on a bifunctional Mo/HZSM-5 catalyst in a packed bed," *Industrial & Engineering Chemistry Research,* vol. 55, no. 37, pp. 9895-9906, 2016.

[5] C. Kloss, C. Goniva, A. Hager, S. Amberger and S. Pirker, "Models, algorithms and validation for opensource DEM and CFD–DEM," *Progress in Computational Fluid Dynamics, an International Journal,* vol. 12, no. 2-3, pp. 140-152, 2012.

[6] C. Goniva, K. Christoph, N. G. Deen, J. A. M. Kuipers and S. Pirker, "Influence of rolling friction on single spout fluidized bed simulation," *Particuology,* vol. 10, no. 5, pp. 582-591, 2012.

[7] A. Hager, C. Kloss, S. Pirker and C. Goniva, "Parallel open source CFD-DEM for resolved particle-fluid interaction," *Proceedings of 9th International Conference on Computational Fluid Dynamics in Minerals and Process Industries,* pp. 1-6, 2012.

[8] K. S. Wong, J. W. Thybaut, E. Tangstad, M. W. Stöcker and G. B. Marin, "Methane aromatisation based upon elementary steps: Kinetic and catalyst descriptors," *Microporous and mesoporous materials,* vol. 164, pp. 302-312, 2012.

[9] N. I. Fayzullaev, B. S. Shukurov and A. O. Normuminov, "Kinetics and Mechanism of the Reaction of Catalytic," *International Journal of Oil, Gas and Coal Engineering,* vol. 5, no. 6, p. 124, 2017.

[10] EU, "Zeocat-3D website," *https://www.zeocat-3d.eu/.*